Architecture-encoded mechanics and communication in microtubules: a multiscale computational study

Architecture-Encoded Mechanics and Communication in Microtubules: A Multiscale Computational Study

*Eric A. Zizzi[†,1], Marco Cannariato[†,1], Marcello Miceli[1,2], Umberto Morbiducci[1,2] and Marco A. Deriu[1]**

[1] Polito[BIO]Med Lab, Department of Mechanical and Aerospace Engineering, Politecnico di Torino, 10129, Turin, Italy

[2] Department of Life Sciences, Università Degli Studi di Modena e Reggio Emilia, Via Campi 103, Modena, 41125, Italy

* Corresponding author: marco.deriu@polito.it

[†] these authors contributed equally

Abstract

The mechanical architecture of microtubules (MTs) is crucial for modulating their functions within cells; however, the effect of varying the number of protofilaments (PF) on the propagation of mechanical signals remains largely unexplored. Nevertheless, MTs assembled in vitro exhibit diverse PF numbers depending on the specific tubulin composition, stabilising agents, and cellular context, suggesting a regulated architectural adaptation. Here, we performed a multiscale computational study integrating molecular dynamics, dynamical network analysis, and elastic network modelling to investigate the influence of the MT architecture on structural communication and mechanics. Our results highlight that an increase in PF number alters tubulin-tubulin contact patterns, reshapes lateral surface hydrophobicity, and modulates the dynamics of a specific unstructured region known as the M-loop. Remarkably, we identified a correlation between the PF number, vibrational path length, and bending stiffness, revealing that MTs with larger architectures propagate mechanical information less efficiently, but offer increased structural support. These findings suggest that MT architecture may serve as a design parameter influencing the propagation of mechanical signals across scales. Moreover, they

may contribute to the emerging field of neuromechanobiology, where MTs are considered potential integrators of mechanical and informational processes within neurons.

Keywords

microtubules, cytoskeleton mechanics, protofilaments, ENM, protein network modelling, molecular dynamics

Introduction

Microtubules (MTs) are hollow tubular assemblies composed of several laterally coupled protofilaments (PFs), which can vary in number based on the tubulin isotype [1], stabilising agents [2,3], cell type, organism, and post-translational modifications [4,5].

MTs play essential roles in cell structure, transport, and mechanotransduction, and their architecture is closely linked to these functions. For instance, a recent study showed that the distribution and architecture of MTs change during the life span of *Plasmodium falciparum***,** the malarial parasite [6], reinforcing the idea that MT architecture is a regulated variable that adapts to cellular needs. In particular, the authors observed how the parasite expresses giant 18PF MTs when it takes an extended, rigid shape. This evidence, coupled with results from investigations of 15PF-shaped MTs in mechanosensory cells [4], corroborates the hypothesis that large MTs are stiffer than the canonical 13PF lattice, and can provide structural support for specific cells [7]. The functional significance of PF architecture is also evident in ciliary axonemes, which are specialized structures found in cilia and flagella whose wall is composed of nine MT doublets, each consisting of a complete 13PF A-tubule and a partial 10PF B-tubule, with a central microtubule pair usually composed of two 13-PF microtubules[8–10]. This organization ensures both structural stability and mechanical efficiency: the 13PF A-tubule provides a rigid scaffold for anchoring dynein arms and other axonemal complexes, whereas the 10PF B-tubule economizes tubulin usage and contributes to the flexibility required for axonemal beating[8,9]. In addition, protofilament-specific patterns of tubulin post-translational modifications further fine-tune the mechanical properties of axonemal MTs and regulate their interactions with motor and regulatory proteins, thereby directly influencing ciliary motility[9,11]. These examples demonstrate how cells control the architecture of their MTs according to specific functional requirements, with larger MTs generally providing enhanced structural support and stiffness, and smaller MTs providing increased flexibility.

Despite the recognised variability in PF numbers and their potential impact on cellular functions[1,12,13], the exact mechanisms by which these variations influence MT mechanics and signal propagation remain unclear[14–16]. Most research has concentrated on specific MT states or geometries, lacking a comprehensive analysis that directly compares how different architectures affect the mechanical

behaviour across scales. This question is particularly relevant in the context of neuromechanobiology, an emerging field that investigates how mechanical forces and cytoskeletal dynamics contribute to neuronal signalling[17–19], development[20], and cognition[21,22].

In this context, multiscale modelling presents a unique opportunity to bridge the gap between molecular interactions within MTs and their macroscopic mechanical properties, allowing for a detailed exploration of how variations in the number of PFs impact MT function.

In the present work, we quantitatively investigate how the MT architecture is linked to its mechanical behaviour through a multiscale computational framework that combines molecular dynamics simulations, dynamic network analysis, and elastic network modelling. Specifically, to cover a wide range of MT sizes including both common MT lattices and rare, specialized assemblies, we focused our study on the 11PF assembly, a specialized structure found e.g. in nematodes and plants[4], the 13PF assembly, which is the most prevalent lattice in eukaryotic cells[23], and the 16PF assembly, a large and highly specialized MT lattice occurring in protists and insects[4]. This allowed us to span a wide range of PF numbers – and, thus, MT sizes – in our investigation, while also relying on available electron microscopy density (EMD) maps [24], which enabled us to reconstruct representative models of MTs characterised by a different numbers of PF starting from experimental data.

We recently applied molecular dynamics (MD) simulations to study tubulin-tubulin interactions within the MT lattice [25,26], providing a detailed view of the local structural and communication dynamics. In addition, we have previously used elastic network modelling to estimate the mechanical properties of cytoskeletal filaments [27–29], which agrees with recent experimental studies on microtubule deformation mechanics [30]. Herein, we investigate MTs with different numbers of PFs to investigate how MT architecture, tubulin-tubulin interactions, and MT mechanics are interlinked.

Our results highlight that changes in the MT wall curvature can be associated with differences in the lateral interaction surface and in its hydrophobicity. Moreover, increasing the number of PFs increases the bending stiffness of the assembly, which is consistent with previous hypotheses[7].

Our study advances our current understanding of how MT architecture influences its mechanical properties, with potential implications for understanding how cells adapt MT functions to meet various physiological demands.

Methods

Preparation and simulation of the models

To study tubulin dynamics within MT sheets representative of different lattices, we started from our previously published methodology[25,26]. In greater detail, we used Protein Data Bank structure 3J6F [31] as a template to construct a 3x4 GDP-bound patch of human αIb-βIII tubulin dimers using homology modelling, as performed in an earlier study of our research group [25] and further illustrated in the Supporting Information. This molecular configuration was regarded as representative of a 13 PF MT wall and will be referred to as MT^{13PF}. To model MT sheets at 11 and 16 PFs, the curvature of this initial MT sheet has been adapted using the ChimeraX software [32] and available EMD maps [24] (accession codes EMD-5191 for the 11:3 lattice and EMD-5196 for the 16:4 lattice). In detail, first the whole MT^{13PF} structure has been fit as a rigid body into the EMD maps. Subsequently, the three PFs have been independently fit into the EMD map. The obtained systems will be referred to as MT^{11PF} and MT^{16PF} and represent the initial structure of 11 and 16PF MT patches. Following the same naming convention and rationale used in our previous works [25,26], we will distinguish between S1, S2 and S3 systems. S1 systems represent MT patches far from the MT seam, i.e. in which the tubulin dimers of the different PFs are laterally aligned. S2 and S3 systems instead refer to MT patches representing the MT seam region, i.e. where one PF (the rightmost in system S2, the leftmost in system S3) is offset by one tubulin subunit with respect to the other two (see Figure 1).

In the case of the MT^{11PF}, the S2 and S3 systems have been modelled following the same procedure as above, but starting from the corresponding S2 and S3 systems of MT^{13PF}. These systems have been constructed as models of the MT seam region. In the case of the 16PF lattice, the S2 and S3 systems have not been modelled as the seam is not present in the 16:4 architecture. All assembled molecular systems were setup, equilibrated and simulated using the following Molecular Dynamics (MD) protocol, as already employed in our previous studies[25,26]: first, we assigned the protonation state of titratable residues using PROPKA[33] predictions corresponding to a pH of 7.4, and parametrized all protein subunits using the AMBER ff99SB-ILDN force field[34]. Additional ligands, namely GTP and

GDP whose coordinates were preserved from the original experimental structure, were parametrized using the General Amber Forcefield (GAFF)[35] after assigning atomic partial charges using the AM1-BCC[36] methodology. Each molecular system was then positioned into a cubic box of size 20 nm x 18 nm x 9 nm filled with explicit TIP3P water and an adequate number of Na^+ and Cl^- ions to ensure system neutralization and a physiological salt concentration of 0.15M. Systems then underwent a 1000-step energy minimization run using the steepest descent algorithm. Finally, three distinct MD simulation replicates were obtained by first equilibrating the systems in the NVT ensemble at 300 K (τ = 1 ps) for 500 ps using the Berendsen thermostat[37]. Then, systems were further equilibrated for 500 ps in the NPT ensemble at a reference temperature of 300K and a reference pressure of 1 bar (τ = 5 ps) using the Berendsen barostat. During both these equilibration runs, we harmonically restrained the positions of all alpha-carbons with a force constant of 1000 kJ/mol nm^2. After equilibration, we ran production MD simulations in the NPT ensemble, using the Particle Mesh Ewald algorithm with a short-range cutoff of 1.2 nm and potential switching at 1.0 nm to treat electrostatic interactions. Van Der Waals interactions were cutoff at 1.2 nm with potential switching at 1.0 nm. To limit the deviation of the sheets from the experimental curvature of the MT during these production runs, we restrained the positions of one β-strand of the tubulin monomers located at the four vertices of the sheets – specifically residues β132-138, β163- 170, β198-203 and α133-140, α165-171, α200-204 – with a force constant of 1000 kJ/mol nm^2. Unlike similar approaches in previous literature [27,28,38], by only restraining the vertices, we did not apply any position restraint to tubulins whose dynamics we analyzed. All simulations were carried out in GROMACS 2021.4 [39], in three replicates for each molecular system.

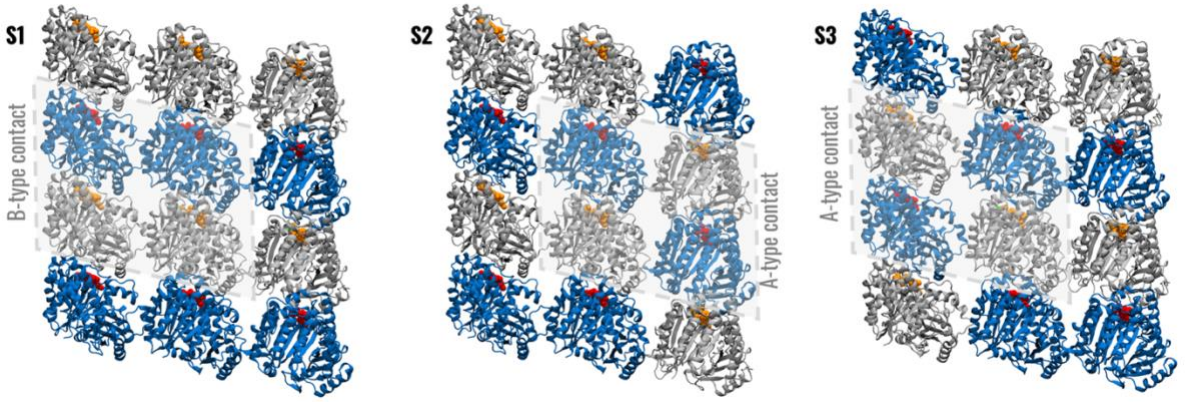

Figure 1 Graphical visualization of the three simulated sheets: S1 is representative of 3 adjacent protofilaments far from the MT seam; S2 and S3 represent the structural discontinuity between adjacent PFs to the left (S2) and to the right (S3) of the MT seam.

S1 systems, which we focussed on herein to investigate the tubulin dynamics within the MT wall with different lattice configurations, were simulated for a total of 500 ns per replica. The rationale of focusing on the dynamics of tubulins in regions far from the seam – represented by the S1 systems – is that no A-type contacts are present in the 16:4 lattice, and that depolymerization is statistically less favorable to initiate at the seam [40]. Also, previous studies have shown that the MT seam does not constitute a mechanically weaker discontinuity with respect to the rest of the lattice[41]. Conversely, in the case of S2 and S3 systems representing regions adjacent to the MT seam, the MD simulations served the purpose of relaxing the systems before extracting conformations for the subsequent ENM-NMA analysis, and these systems were thus simulated for 200 ns per replica.

Analysis of MD simulations

The MD simulations of MT^{11PF}, MT^{13PF}, and MT^{16PF} were analysed as follows. The structural stability of the system in each of the three replicas was quantified by evaluating the root-mean-squared deviation (RMSD) of the backbone atoms of the sole central tubulin heterodimer as well as of the whole system with respect to their initial coordinates. Once the equilibrium portions of the simulations were identified, the respective trajectories were concatenated and sampled every 50 ps to perform further analyses. The most flexible regions were identified by computing the root-mean-squared fluctuations (RMSF) of Cα atoms, while per-residue secondary structure probability was computed using the STRIDE software package [42]. We subsequently analysed the interactions between the central tubulin heterodimer and the

ones of adjacent PFs by means of the frequency of contacts [25,26], and computed the contact surface between the central tubulin heterodimer and the neighbouring ones [26]. We also inspected the percentage of the hydrophobic area within the lateral buried surface. In addition, we used the PLIP[43] tool to determine the nature of the interactions between specific amino acids of the central tubulin heterodimer and adjacent PFs, and further calculated the electrostatic potential map as follows: first, we extracted frames every 1 ns from the concatenated equilibrium trajectory, and then performed clustering using the gromacs *cluster* tool, using the gromos clustering method and a cutoff of 0.15 nm, after RMSD-fitting the frames based on the positions of alpha carbons of the central tubulin dimer. We then used the centroid of the most populated cluster as the representative equilibrium conformation, and calculated the electrostatic potential map using ABPS[44], imposing an ionic strength of 150 mM, a solvent dielectric constant of 78.54 and a protein dielectric constant of 1.0.

The structural communication within MT^{11PF}, MT^{13PF}, and MT^{16PF} has been investigated using the dynamic network analysis approach [45], as done in our previous studies[25,26]. The term structural or mechanical communication refers to the possible ways in which the vibrational stimuli can propagate inside the protein structure thanks to dynamic interaction between amino acids. After obtaining a network representation of the molecular structure, we calculated the following metrics from the network analysis: the *degree of centrality* represents how important a given node is locally in the network, and can be calculated as $dg_i = \sum_{i \neq j} A_{ij} w_{ij}$, where A is the adjacency matrix defining the graph and w_{ij} is the weight of the edge connecting node i with node j. The *betweenness centrality* (of a node or edge) is a metric representing the importance of a given node or edge in connecting distant parts of the network. In other terms, it is related to how many shortest pathways between any two nodes include the given node or edge. It is calculated as $b_i = \frac{1}{C} \sum_{s,t \in V} \frac{\sigma(s,t|i)}{\sigma(s,t)}$ where $\sigma(s,t)$ represents the total number of shortest paths between two nodes *s* and *t*, and $\sigma(s,t|i)$ is the number of such shortest paths involving node (or edge) *i*. C is a normalization factor equal to $\frac{(n_n-1)(n_n-2)}{2}$ for node betweenness centrality and $\frac{n_n(n_n-1)}{2}$ for edge betweenness centrality, where n_n is the number of nodes in the graph. Lastly, the *closeness centrality* of a node *i* is calculated as the reciprocal of the sum of the length $d(j,i)$ of the

shortest paths between node *i* and all other reachable nodes N, according to the formula $C_i = \frac{N-1}{\sum_{j=1}^{N-1} d(j,i)}$.

The closeness centrality of each node in the network has been computed to gain information about the length of paths connecting one node to the rest of the network. In this case, higher average closeness centralities are associated with networks where the transfer of vibrational information is more efficient. Three-dimensional representations of receptor structures were rendered in VMD software [46]. RMSD, RMSF, and solvent accessible surface area were computed through the GROMACS analysis tools. Contact frequencies and probability of secondary structures were computed through custom-made Python scripts and using the MDAnalysis library.

Elastic network modelling of MT models

We followed the procedure described in our previous study [26] to build three MT models for each of the architectures under study, i.e., 11:3PF, 13:3PF, and 16:4PF, starting from tubulin conformations derived by the MD simulations of MT^{11PF}, MT^{13PF}, and MT^{16PF}, respectively. For this purpose, previously published EMD maps (accession codes EMD-5191 for the 11:3 lattice, EMD-5193 for the 13:3 lattice, and EMD-5196 for the 16:4 lattice [24]) were exploited to reconstruct 400 nm-long MTs. One MT model was obtained from each S1-3 replica, obtaining a total of 3 MT models per architecture. The MT models were analysed using ENM-NMA, which was performed using an in-house fortran77 code [27]. After a visual inspection of the normal modes, the frequencies corresponding to the first bending, torsion, and stretching motions were considered to predict the bending, torsional, and stretching stiffness, as done in previous studies [27,47]. Briefly, the bending stiffness (flexural rigidity, k_{Eb}), stretching stiffness (k_E) and torsion stiffness (k_G) can be extracted starting from the eigenvalues of the corresponding normal modes using the linear elastic beam theory: for small deformations, wave equations can be used to describe the bending, stretching and torsion displacements, leading to the following relationships between the wave numbers (w_n) and the angular frequencies (ω_n) of the n-th mode:

$$\rho\omega_n^2 = k_{Eb} w_n^4 \quad (1)$$

$$\rho\omega_n^2 = k_E w_n^2 \quad (2)$$

$$\rho_v I\omega_n^2 = k_G w_n^2 \quad (3)$$

Where I is the second moment of area of the cross-sectional area, and ρ and ρ_v are the mass per unit length and per unit volume of the filament, respectively. The wave numbers can be then determined for bending modes as:

$$\cos(w_n L_{MT}) + \cosh(w_n L_{MT}) = 1 \quad (4)$$

Where L_{MT} is the length of the microtubule.

Conversely, for modes corresponding to stretching and torsion, the wave number can be calculated (for the *n-th* mode) using:

$$w_n = \frac{n\pi}{L_{MT}} \quad (5)$$

Once the wave numbers have been calculated, k_{Eb} , k_E and k_G can be calculated using equations (1), (2) and (3) after calculating the angular frequencies ω_n from the eigenvalues of the modes. Finally, the stiffnesses can be converted to mechanical moduli using the following relationships: the bending modulus E_b is given by:

$$E_b = \frac{k_{Eb}}{I} \quad (6)$$

The stretching modulus, E, is given by the ratio between the stretching stiffness k_E and the cross-sectional area of the filament, A, multiplied by L_{MT}:

$$E = \frac{k_E}{A} L_{MT} \quad (7)$$

Lastly, the shear modulus is directly proportional to the torsion stiffness, k_G , and is equal to:

$$G = \frac{k_G}{J} \quad (8)$$

Where J is the polar moment of inertia. Details of the MT reconstruction and NMA are provided in the Supporting Information. Compared to previous studies, three models were built for each MT lattice using different tubulin conformations extracted from MD sampling. A visual representation of the analyzed molecular systems and methodological approaches is provided in figure S1 of the Supporting Information.

To evaluate possible quantitative relationships between the number of PFs and the mechanical parameters of the MT described above, we fitted and compared three different scaling models, namely

a power-law model in the form $Q(N) = \alpha N^b$, a linear model in the form $Q(N) = \alpha N + b$ and an exponential model $Q(N) = \alpha e^{bN}$. The best model was selected based on the log-likelihood. Details on the methodology for determining the best scaling models and estimating uncertainties can be found in the Supporting Information.

Results

The RMSD analysis, representing a quantitative assessment of conformational stability (Figure S2 and S3), led to the first 100 ns of each MD simulation being regarded as structural equilibration, and thus discarded from further analyses; the conformational stability of the central tubulin dimer in the remainder of the MD simulations was confirmed by means of a cluster analysis, performed using the single linkage algorithm and the RMSD between the C_αs as the metric (cutoff = 0.15 nm). The conformational stability regions of the S1 systems were finally concatenated to obtain 1.2 μs long trajectories for MT^{11PF}, MT^{13PF}, and MT^{16PF} that were subsequently analysed further.

M-loop flexibility in the different MT lattices

Since the conformation and flexibility of the M-loop (residues 272 to 288)[24] are pivotal for MT assembly and stabilisation, this was the first aspect that we investigated. The RMSF analysis highlighted no particular difference in flexibility in the αM-loop region, whereas a different flexibility profile of the βM-loop was evident (Figure S4).

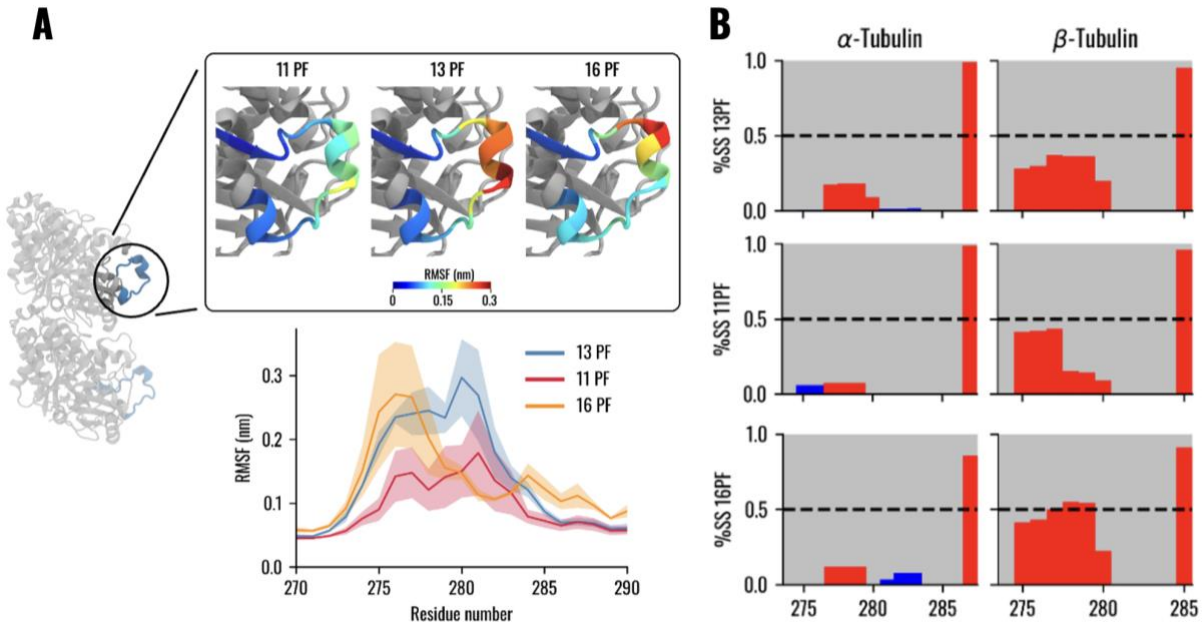

Figure 2. M-loop flexibility in the three MT lattices. (A) RMSF of the central β-tubulin M-loop in MT^{11PF}, MT^{13PF}, and MT^{16PF}. Mean value across the three replicas is represented with a continuous line, whereas the shaded region represents the region within one standard deviation from the mean. At the top, a visual representation of the mean RMSF is shown on the cartoon representation of the βM-loop. The structure of the β-tubulin is the starting conformation of MT^{13PF}. Full tubulin dimer shown in light grey on the left with the location of the M-loops highlighted for visual reference. (B) Secondary structure probability for M-loop residues. Helices are colored in red, strands in blue, and coils in grey.

In particular, the RMSF of MT^{11PF} was lower than that of MT^{13PF}, especially at the N-terminus. In contrast, the βM-loop of MT^{16PF} was as flexible as that of MT^{13PF} at the N-terminus, while its fluctuations were remarkably reduced in the C-terminal region (Figure 2A). In comparison, the H1′-S2 loop (residues 53-64) and the H2-S3 loop (residues 81-91), both known to also be involved in the lateral PF coupling together with the M-loop[24], showed no remarkable differences in secondary structure or RMSF trends in the different MT architectures (Supporting Figures S5, S6). Instead, while the αM-loop remaining mainly unstructured in all systems, the βM-loop was characterised by an increased probability of forming helices (Figure 2B). An increase in the folding probability, especially at the C-terminus, was found in MT^{16PF}, whereas in MT^{11PF} we noticed a slight increase in the helix content at residues 275-277 as well as an unfolding of residues 278-280. Interestingly, the residues which displayed a reduced flexibility in the MT^{16PF} architecture were completely unstructured in all systems. These findings indicate that variations in protofilament number influence the structural dynamics and secondary structure propensity mainly of the M-loop, with MT^{16PF} in particular showing enhanced stabilization at its C-terminal region. Given the established role of the M-loop in mediating lateral

interactions between protofilaments[24,48,49], these observations provide a structural basis for further examining the differences in lateral coupling between adjacent PFs across MT^{11PF}, MT^{13PF}, and MT^{16PF} architectures more in depth.

Lateral coupling of PFs

Since it has been shown that the main actors of PFs lateral coupling are the M and H2-S3 loops in all the investigated MT architectures [24], we subsequently focused on the lateral interactions between tubulin dimers in MT^{11PF}, MT^{13PF}, and MT^{16PF}. Interestingly, the laterally buried surface area between tubulins was not linearly related to the number of PFs.

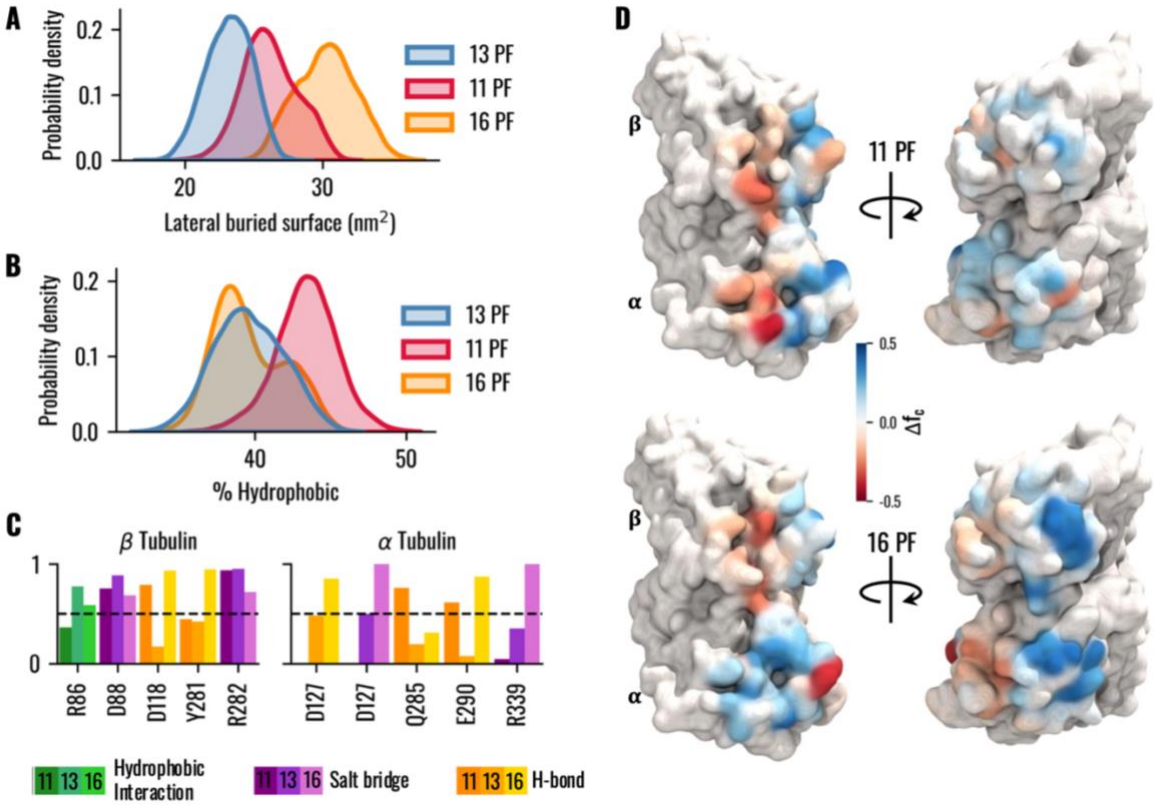

Figure 3 (A) lateral buried surface. (B) percentage of hydrophobic area in the total lateral buried surface. (C) Probability of interactions formed by specific amino acids of the central tubulin dimer with adjacent PFs. Hydrophobic interactions shown in green shades, salt bridges shown in purple shades and hydrogen bonds shown in orange/gold shades. Each group of bars represent the probability of the given interaction in the three systems (11PF leftmost bar, 13PF central bar, 16PF rightmost bar). (D) visual representation of the difference in frequency of contacts between MT^{11PF} and MT^{13PF} (top) and between MT^{16PF} and MT^{13PF} (bottom). Positive (blue) values indicate an increase in frequency with respect to MT^{13PF}, while negative (red) values reduction in frequency. The side exposing the intermediate domain is shown on the left, and the one exposing the N-terminal domain on the right.

288 MT^{13PF} showed the lowest amount of buried area, MT^{16PF} the highest (Figure 3A). In terms of surface
289 characteristics, MT^{13PF} and MT^{16PF} showed a comparable fraction of hydrophobic buried surface,
290 whereas in the MT^{11PF} architecture the hydrophobic portion of the lateral surface was higher (Figure
291 3B). Previously, we showed that the H3 and H9 helices, M, H1'-S2, and H2-S3 loops were characterised
292 by high contact frequency in MT^{13PF} [25]. To also investigate the role of electrostatics in mediating lateral
293 PF-PF coupling, we computed the electrostatic potential map on the surface of the central tubulin dimer
294 in the sheet, in the three architectures (Figure S7). The results highlighted qualitative differences in
295 surface electrostatic potential in the inter-protofilament contact regions between the 11PF, 13PF and
296 16PF configuration: overall, the 11PF configuration featured the largest number of neutral patches in
297 the lateral PF-PF contact region, and the surface of the 11PF βM-loop in particular showed an increased
298 number of locally neutral and positive patches with respect to the 13PF and 16PF configurations,
299 consistent with the reduced flexibility observed in the RMSF analysis. The differences in surface
300 potential between the 13PF and 16PF architectures instead were more subdued, with no evident
301 differences in the βM-loop region.
302 The analysis of the contact frequencies in MT^{11PF} highlighted no remarkable differences at the N-
303 terminal domain, whereas at the intermediate domain, an increase in contacts was observed towards the
304 MT lumen, as well as a loss of contacts moving away from the MT lumen. Regarding MT^{16PF}, at the
305 intermediate domain, there were minimal differences in β-tubulin compared to MT^{13PF}, but contact
306 frequencies were generally higher in α-tubulin, with the only exception being a small region of the M-
307 loop. In contrast, at the N-terminal domain, a gain of contacts towards the outside of the MT wall was
308 identified in both α- and β-tubulins. A visual representation of MT^{11PF} and MT^{16PF} contact frequency
309 differences with respect to MT^{13PF} is shown in Figure 3D. The analysis of specific interacting amino
310 acid patches (Figure 3C) revealed a decreased hydrophobic interaction of βArg86 in the 11PF
311 configuration, increased hydrogen bonding of βAsp118 in the 11PF and 16PF architectures, and
312 enhanced formation of hydrogen bonds of βTyr281 in the 16PF configuration. On the α-tubulin, the
313 formation of hydrogen bonds of αAsp127 was lost in the 11PF configuration, and greatly reduced for
314 αGlu290 in the 13PF configuration, whereas αGln285 formed hydrogen bonds with neighbouring PFs
315 mainly in the 11PF configuration compared to other architectures. αAsp127 formed salt bridges with

neighbouring PFs mainly in the 16PF architecture, and moderately in the 13PF architecture. No salt bridge was instead observed for this residue in the 11PF configuration. Also, the probability of forming salt bridges of αArg339 noticeably increased with the number of PFs.

Overall, the variations in contact frequencies and interaction probabilities among the MT^{11PF}, MT^{13PF}, and MT^{16PF} architectures originate from the distinct packing of tubulin dimers in adjacent protofilaments, driven by the curvature of the MT wall imposed by different protofilament numbers. This structural feature is expected to influence the propagation of mechanical cues within the lattice, which we therefore investigated using dynamic network analysis.

Structural communication in the MT lattices

To investigate the relationship between MT architecture and mechanical cue propagation within the MT wall, we performed a dynamic network analysis on the three systems. As resulted from earlier studies [25], the degrees of centrality of β-tubulin and α-tubulin are similar, with slightly higher centralities for β-tubulin. In the present investigation, the same pattern was observed in all three MT lattices, indicating that the local dynamic influence of tubulin amino acids was similar in MT^{11PF}, MT^{13PF}, and MT^{16PF} (Figure 4A).

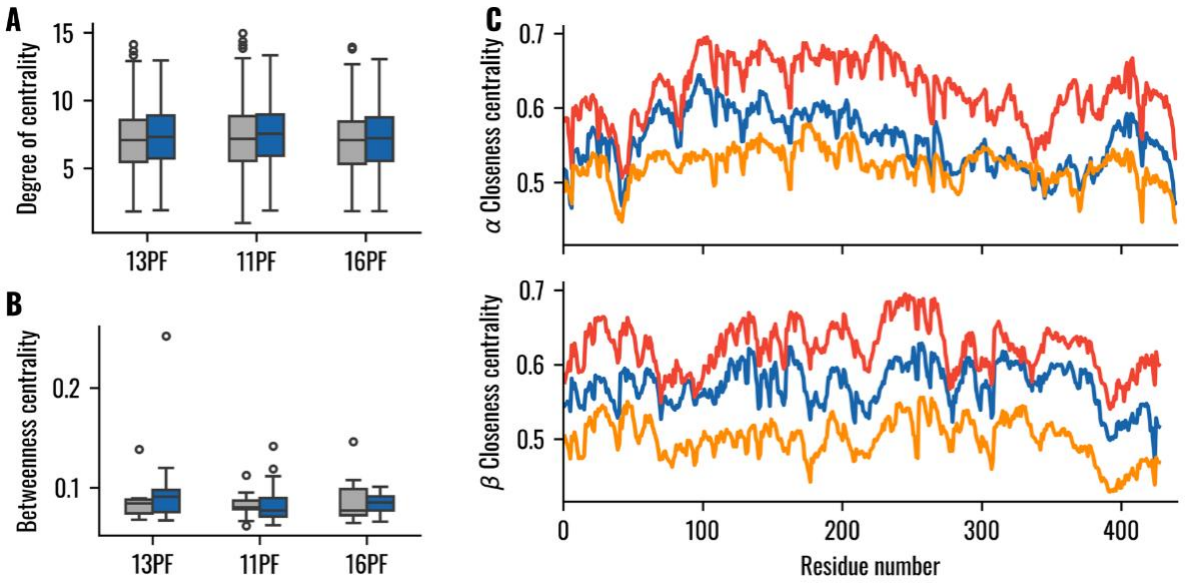

Figure 4 Network analysis of the different MT architectures. (A) Boxplots showing the degree of centrality of the central tubulin heterodimer nodes. Grey boxplots show α-tubulin nodes, while blue boxplots the β-tubulin nodes. (B) Boxplots showing the nodes betweenness centralities for the central tubulin heterodimer. Grey boxplots show α-tubulin nodes, while blue boxplots the β-tubulin nodes. (C) Closeness centrality of the central tubulin heterodimer residues. MT^{16PF}, MT^{13PF}, and MT^{11PF} are coloured in orange, blue, and red, respectively.

We subsequently plotted the betweenness centrality of the nodes against the node rank to define a threshold, that is, the knees of the curves for the MT^{11PF}, MT^{13PF}, and MT^{16PF} systems. The three thresholds were similar (Figure S8), and the lower one was selected. Node betweenness centrality values above the selected threshold were considered in the subsequent analyses. First, we inspected the curve of α- and β-tubulin node betweenness centralities versus their rank, and observed that in the case of β-tubulin, the first-ranking nodes had the lowest betweenness in MT^{16PF} (Figure S9). Comparing the distribution of the betweenness centrality of α- and β-tubulins, MT^{11PF} displayed a higher importance of β-tubulin nodes, as in MT^{13PF}. In contrast, in the case of MT^{16PF}, the median of β-tubulin distribution was still higher than that of α-tubulin distribution, but the highest importances were observed for α-tubulin (Figure 4B). Details of the distributions of degrees of centrality and betweenness centralities are reported in the Supporting Information (Figure S10). Finally, we computed the closeness centrality as a metric indicating how "close" a certain node is to the rest of the network. The distribution of the closeness centrality values within tubulins was similar in the three architectures; however, higher centralities were observed in MT^{11PF}, whereas the lowest centralities were observed in MT^{16PF} (Figure 4C). Therefore, in general, we found that the shortest communication paths increase with the number of PFs. This was confirmed by the computation of the wiener indexes in the three networks (Figure S11), which also increased with the number of PFs. Interestingly, the M-loops were regions of low centrality in all systems, but the αM-loop importance was higher in MT^{11PF} (Figure S12). Moreover, helix H8, which mediates vertical interactions between tubulins [25], was characterised by higher closeness centrality in the intra-dimer interface than in the inter-dimer interface, particularly for MT^{16PF}.

Elastic Network Modelling of the MT models

The mechanical properties of MTs were inferred using the ENM-NMA approach [27,28]. From the longitudinal bending, torsion, and stretching vibrational modes, mechanical parameters such as bending (κ_{Eb}), torsion (κ_G), and stretching (κ_E) stiffnesses were estimated. The results obtained using this methodology were consistent with previous experimental data found in the literature [30,50–52] (Figure 5A,E). We found that the bending and torsional stiffnesses significantly increased with the number of

PFs, whereas minimal differences were observed between the stretching stiffnesses (Figure 5B-D, significant if $p<0.05$ with Mann-Withney U test).

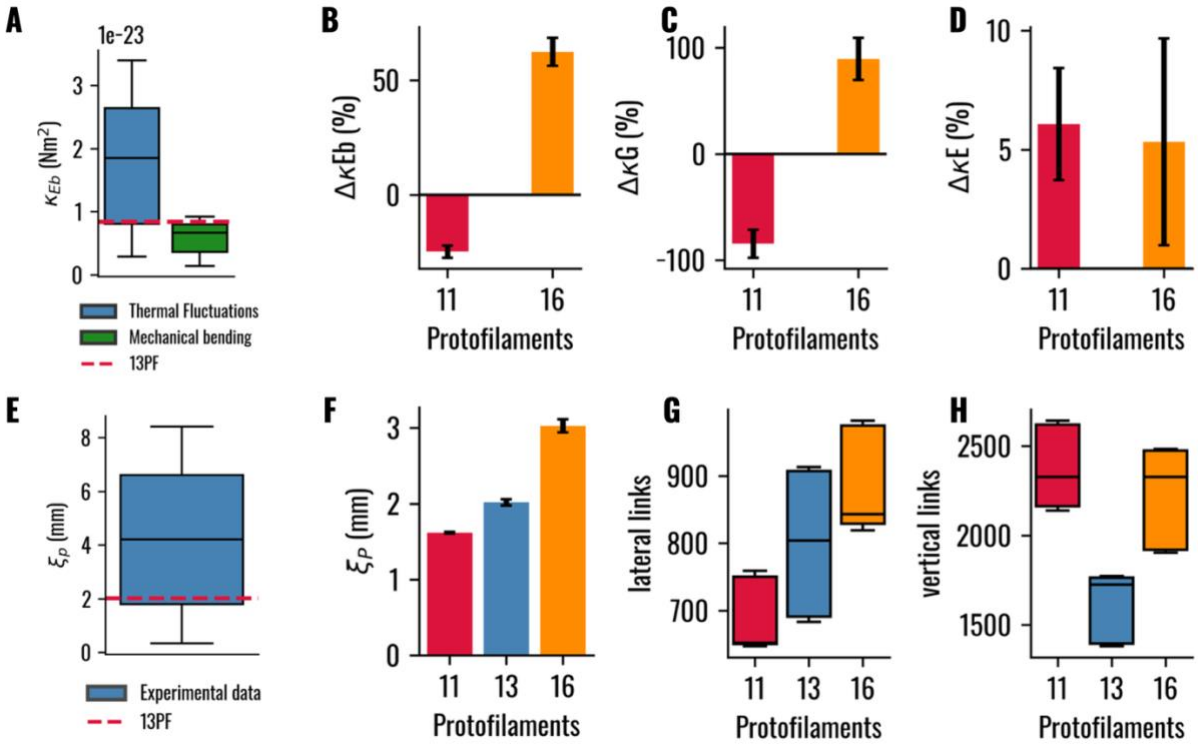

Figure 5 Elastic Network Modeling of the three MT lattices. (A) Comparison between the mean bending stiffness from this work (dashed line) and the experimental data found in [30,50–52]. (B-D) Bending (B), torsional (C), and stretching (D) stiffnesses of the 11PF and 16PF MT architectures expressed as the percentage of variation from the 13PF MT. The bars show the standard deviation across the three ENMs. (E) Comparison between the mean persistence length of the 13PF MT from this work (dashed line) and the experimental data found in [30,51].(F) Persistence length of the 11PF, 13PF, and 16PF MT architectures, where the bars represent the standard deviation across the three ENMs. (G, H) Number of links, in the ENMs of the 11PF, 13PF, and 16PF MT architectures, connecting vertically (G) and laterally (H) coupled tubulins.

Thus, given the direct proportionality between the bending stiffness and the persistence length of the MT, the latter also increased with the number of PFs, reaching a value of 3 mm in the case of a 16PF lattice (Figure 5F). The persistence length value obtained for the 13PF system was also found to be in good agreement with previously reported data[30,51] (Figure 5E).

We then determined the mechanical moduli, that is, the bending (E_b), shear (G), and Young's (E) moduli, which characterise the material properties: no significant differences were observed between the shear moduli, whereas the Young's and bending moduli decreased with the number of PFs (Figure S13). Interestingly, these findings highlight how geometric effects (increase of the MT radius) dominate over variations of material properties (increase of the bending stiffness κ_{Eb}) as the number of protofilaments

increases: the bending modulus (E_b) decreases with the number of PFs since the second moment of area of the MT, which scales with the fourth power of the radius, increases more rapidly than the bending stiffness κ_{Eb} (see Figure S14).

Notably, the bending and Young's moduli were approximately the same in all the architectures; thus, the Euler–Bernoulli approximation could be used to model the MTs at the considered length, under the hypothesis of a limited effect of shear between PFs on the bending deformation. Starting from the mechanical moduli, we inferred the lengths at which the deformation due to shear was 5% and 50% of the total (Figure S15). The length at which the shear contribution was 5% was ~460 nm for the 11PF and 13PF lattices, while it reached ~550 nm for the 16PF MT. Therefore, the shear contribution of the 16PF architecture is significantly higher when considering the same MT length. Interestingly, considering the length/radius ratio at which the shear contribution is 5%, we obtained a value of ~43 in the case of the 13PF and 16PF lattices, while it was ~52 for the 11PF architecture. While a precise quantification of the shear stresses experienced my MTs in vivo remains elusive, earlier studies[53,54] confirmed that shear stresses in the range of 0.05 to 23 Pa[54–57] induce microtubule alignment and reorganization, affecting cell shape and migration: for instance, in cardiomyocytes and endothelial cells subjected to shear stresses, MTs act as compression-resistant elements[58–60]. Taken together, these results further corroborate the hypothesis that PF architecture may play an active role in mechanotransduction. In particular, the enhanced shear contribution of 16PF lattices may amplify deformation under flow, potentially affecting force transduction and remodelling dynamics, whereas 11PF lattices appear intrinsically more resistant to shear deformation.

We finally related the differences in the mechanical moduli to the topologies of the ENMs built using the MT models of different lattices. We found that the number of links in the ENMs between laterally coupled tubulins increased with the number of PFs, providing a structural explanation to the observed increase in bending stiffness and persistence length. Conversely, the links between vertically coupled tubulins were similar between the 11PF and 16PF MTs, with an increase for the 13PF lattice (Figure 5G, H). Overall, we observed that the mechanical parameters such as κ_{Eb}, κ_G, E_b and E scale differently with increasing numbers of PFs in the microtubule (Figure S16), but further studies are required to

precisely determine the nature of such scaling behaviour and to formulate hypotheses regarding the mechanistic underpinnings of the observed trends.

Discussion

Although several studies have documented the existence of MTs with different lattice architectures, the structure–function relationship underlying this variability remains incompletely understood. Previous evidence supports the hypothesis that MT architecture adapts to fulfil specific cellular functions. Given the mechanical support role of MTs, it has been hypothesised that variations in PF number modulate their mechanical properties. In this work, we provided a detailed mechanical characterisation of MTs with distinct architectures, focusing on how tubulin-tubulin interactions vary across lattices and how these variations propagate at higher scales, impacting mechanical behaviour.

Our results show that the main changes in tubulin flexibility are localised to the βM-loop (Figure 2). Specifically, we found it to be partially stabilized in the MT^{16PF} architecture, whereas in MT^{11PF} the βM-loop was fully stabilized. Interestingly, the reduction in βM-loop flexibility and its partial structuring have also been observed in the presence of taxol [26], which is known to promote the formation of MTs with less than 13 PFs [3]. However, we underline how the partial folding in MT^{11PF} involved different residues than those in the taxol-driven scenario.

Our observations are consistent with the idea that MTs may sample a range of accessible architectural states defined at the level of individual tubulin dimers and at the level of their supramolecular lattice architecture. Despite involving different residues, the observed similarities between the MT^{11PF} configuration and the taxol-stabilised state suggest that ligand binding might shift the system toward one of multiple accessible architectural states, a mechanism also known as *conformational selection*. Thus, rather than imposing an artificial conformation, specific stabilising agents may act by selecting and reinforcing specific lattice organisations within this landscape. Distinct protofilament numbers may correspond to discrete, metastable architectural states that differ in local flexibility, inter-dimer contacts, and dynamic communication properties. By stabilising one of these accessible states, ligands such as taxol may shift the equilibrium toward specific MT architectures that would otherwise be transient or

energetically disfavoured under physiological conditions. Indeed, studies have shown that the number of protofilaments is set early during MT formation *in vivo*, primarily during the initial tubulin nucleation and sheet closure phase, rather than through remodelling of the conformation of a pre-existing lattice[61,62]. This has been shown to occur mainly through the stabilisation of early tubulin assemblies by binding agents which promote specific tubulin-tubulin interactions[26,63,64], whereas in the absence of such ligands tubulin *in vitro* assembles freely into microtubules composed of 9 to 16 protofilaments[65].

This concept of ligand-guided conformational selection could help explain the context-dependent efficacy or resistance observed with MT-targeting agents, depending on whether a given cell type naturally explores—or avoids—the ligand-favoured state. The βM-loop conformational rearrangements were also associated with differences in the lateral coupling of tubulins, considering different PF numbers (Figure 3). In the largest MT lattice, a wider laterally buried surface was observed due to the involvement of an additional interaction site including helix H3 [24]. However, the contacts were stabilised on average in the intermediate domain of the sole α-tubulin. In this context, this study shows that the recruitment of additional contacts is reflected in the increase in the lateral buried area. Although MT^{11PF} showed loss of contacts in H9 and subtle changes in the N-terminal domain, its laterally buried surface was slightly increased with respect to MT^{13PF}, along with the hydrophobic contribution. Therefore, the width and nature of the lateral tubulin-tubulin contacts change in the different architectures to provide stability to the MT lattice. This is consistent with studies exploring the role of tubulin-tubulin contact discontinuities, arising e.g. due to lattice defects, in altering overall MT mechanics: missing dimers, dislocations and tubulin-tubulin contact mismatches have been shown to weaken the lattice[66–68] by locally concentrating mechanical stresses[69,70], thereby increasing the susceptibility of the MT to damage. Instead, the discontinuity at the MT seam does not appear to be mechanically weaker than the rest of the lattice[41,71].

Analysis of the degree of centrality showed that the local influence of residues belonging to α- and β-tubulin was similar in the three architectures (Figure 4A). For MT^{16PF}, the betweenness of nodes in α-tubulin was higher, which can be related to the increase in the contact frequencies of α-tubulin residues, resembling the results obtained in the presence of taxol [26]. This observation confirms the relationship between the stability of lateral contacts and the transfer of vibration within the MT, but also suggests

that taxol might induce lattice stabilisation through a combination of mechanisms, apart from the longitudinal lattice expansion, that are also partially adopted to stabilise MT lattices other than the classical 13:3. Finally, the analysis of the closeness centrality (Figure 4C) highlighted that the vibrational path lengths, i.e. the communication pathways in the MT along which mechanical vibrations can propagate, were on average shorter in MTs with lower PFs numbers.

Thus, mechanical communication within lattices with fewer PFs could be said to be more "efficient", in the sense that vibrational signals propagate through more correlated and shorter pathways. As a result, smaller MT architectures might be better suited for rapid mechanical signalling, while larger MTs are structurally optimized to withstand sustained mechanical loads. In particular, large MTs are hypothesised to be employed by cells to provide mechanical support for maintaining shape [6] or resisting deformation under stress [4].

This dual behaviour reinforces the idea that MT architecture is not a passive structural feature, but rather a tunable parameter that balances mechanical sensitivity and robustness depending on functional demands. This view is consistent with previous proposals that microtubules can act as mechanical force sensors [72] , and it encourages further investigation into whether architectural tuning may also influence intracellular communication and mechanoresponsive behaviour. Such architectural tuning aligns with the principles of neuromechanobiology, where cytoskeletal elements are increasingly recognised as integrators of mechanical and informational processes in the nervous system [21,22].

Our results are consistent with these hypotheses, as the bending stiffness of MTs increased with the number of PFs. This effect appears to stem from an increased resistance to inter-protofilament shear—i.e., torsional stiffness (Figure 5B–D)—rather than differences in intrinsic material properties, as the shear moduli were not statistically different (Figure S13). This mechanical response reflects architectural differences in the topology of the elastic network models (Figure 5G–H).

Accordingly, the shear contribution to bending was higher in the MT^{16PF} compared to the 13PF and 11PF lattices (Figure S15). However, the increased bending stiffness observed between the 13PF and 16PF lattices primarily results from their different diameters, as confirmed by the similar length-to-radius ratio at which the shear contribution accounts for 5% of the total deformation (Figure S15). In

contrast, the higher ratio observed in the 11PF architecture indicates a distinct network topology that alters the shearing response.

Thus, while the MT^{16PF} is characterised by more inter-PF contacts that enhance lattice stability and bending resistance, its shearing behaviour remains comparable to that of the 13PF lattice. By contrast, the 11PF lattice exhibits a qualitatively different shearing pattern, which aligns with its unique hydrophobic profile in lateral interactions. Interestingly, these findings suggest that MT architectures represent design solutions evolved to optimize specific mechanical tasks: lower PF numbers favour efficient transmission of mechanical signals through correlated pathways, whereas higher PF numbers provide increased resistance to deformation and enhance lattice robustness. Notably, as the number of protofilaments increases, a competing effect emerges between material properties and geometrical properties, whereby the overall bending modulus decreases despite increased structural connectivity and bending stiffness. Such trade-off between stability and flexibility provides a framework for optimizing mechanical properties through structural design. Considering the preliminary trends that we were able to observe in the present study, a more in-depth investigation of how the mechanical characteristics of MTs scale with increasing numbers of PFs warrants further experimental and computational studies, potentially covering a wider range of MT architectures. This would allow to reconstruct quantitative relationships between MT architecture and key mechanical parameters, thereby further elucidating the biophysical underpinnings of MT mechanics.

The concept of architecture-encoded function also opens new directions in biological understanding and biomaterials design. From a biological standpoint, cells might leverage PF variability to spatially modulate MT mechanics according to local demands, such as rigidity in the axon shaft versus signal responsiveness in dendritic spines.

From an engineering perspective, our approach demonstrates that combining atomistic simulations with ENM/NMA can guide the rational design of bioinspired filaments with tailored mechanical responses. Future extensions of this framework may include ligand binding, isotype substitution, or post-translational modifications to explore how additional regulatory layers integrate into the architecture-function paradigm.

Conclusions

In this study, we conducted a multiscale computational analysis to investigate how MT architecture influences its mechanical properties and internal mechanical cue propagation dynamics. By focusing on experimentally observed MT lattices with varying protofilament numbers, we explored how differences in tubulin-tubulin interactions relate to changes in lattice curvature, structural signalling efficiency, and bending stiffness. Our results support a model in which increased PF number enhances MT rigidity, consistent with previous literature, while reduced PF number favours more efficient mechanical communication.

Beyond structural and mechanical implications, these findings may inform emerging perspectives in neuro-mechanobiology, where microtubules are increasingly considered potential mediators of information transfer within cells.

Given their highly charged surfaces and intrinsic vibrational dynamics, changes in lattice architecture, such as those driven by PF number, could influence mechanical signalling, electrostatic and field-based interactions.

This raises the challenging possibility that MTs might contribute to subcellular information-processing functions, including neuronal signalling and potentially memory-related processes.

This line of reasoning aligns with recent biophysical models exploring microtubules' dynamic and vibrational properties as potential conduits for intracellular computation [73]. Our findings contribute to a growing body of evidence suggesting that MTs possess an architectural and dynamic complexity that could support information-modulatory roles beyond purely structural or mechanical functions. Whilst speculative, this hypothesis opens exciting avenues for future investigation at the interface between mechanics, electrobiology, and cognitive biology. It is worth highlighting, however, that further experimental validation is needed to clarify the mechanistic links between MT architecture, its dynamic behaviour, and its functional role in complex cellular systems.

Data Accessibility

A Supporting Information file is available, containing details on the MD and ENM methodology and supplementary figures S1-S16. In addition, all files necessary to replicate the findings reported herein, namely system topologies, starting structures and parameter files for the MD simulations as well as starting files and templates to reconstruct the MT rings, can be found on Zenodo at https://doi.org/10.5281/zenodo.16961992 .

Acknowledgements

We acknowledge ISCRA for awarding this project access to the LEONARDO supercomputer, owned by the EuroHPC Joint Undertaking, hosted by CINECA (Italy).

Author Contributions

The manuscript was written through contributions of all authors. EAZ, MC and MM conceptualized the study, carried out the molecular modelling and simulations, analysed and interpreted the results. UM and MAD conceptualized and supervised the work and interpreted the results. All authors have given approval to the final version of the manuscript. †These authors contributed equally.

Conflict of Interest Statement

The authors declare no competing interests.

Funding Statement

The research leading to these results has received funding from the European Union—NextGenerationEU through the Italian Ministry of University and Research under PNRR—M4C2-I1.3 Project PE_00000019 “HEAL ITALIA” to M.M. and U.M., CUP E93C22001860006. The views and opinions expressed are those of the authors only and do not necessarily reflect those of the European

Union or the European Commission. Neither the European Union nor the European Commission can be held responsible for them.

References

(1) Ti, S.-C.; Alushin, G. M.; Kapoor, T. M. Human β-Tubulin Isotypes Can Regulate Microtubule Protofilament Number and Stability. *Developmental Cell* **2018**, *47* (2), 175-190.e5. https://doi.org/10.1016/j.devcel.2018.08.014.

(2) Matesanz, R.; Rodríguez-Salarichs, J.; Pera, B.; Canales, Á.; Andreu, J. M.; Jiménez-Barbero, J.; Bras, W.; Nogales, A.; Fang, W.-S.; Díaz, J. F. Modulation of Microtubule Interprotofilament Interactions by Modified Taxanes. *Biophysical Journal* **2011**, *101* (12), 2970–2980. https://doi.org/10.1016/j.bpj.2011.11.005.

(3) Díaz, J. F.; Valpuesta, J. M.; Chacón, P.; Diakun, G.; Andreu, J. M. Changes in Microtubule Protofilament Number Induced by Taxol Binding to an Easily Accessible Site. *Journal of Biological Chemistry* **1998**, *273* (50), 33803–33810. https://doi.org/10.1074/jbc.273.50.33803.

(4) Chaaban, S.; Brouhard, G. J. A Microtubule Bestiary: Structural Diversity in Tubulin Polymers. *MBoC* **2017**, *28* (22), 2924–2931. https://doi.org/10.1091/mbc.e16-05-0271.

(5) Janke, C.; Magiera, M. M. The Tubulin Code and Its Role in Controlling Microtubule Properties and Functions. *Nat Rev Mol Cell Biol* **2020**, *21* (6), 307–326. https://doi.org/10.1038/s41580-020-0214-3.

(6) Ferreira, J. L.; Pražák, V.; Vasishtan, D.; Siggel, M.; Hentzschel, F.; Binder, A. M.; Pietsch, E.; Kosinski, J.; Frischknecht, F.; Gilberger, T. W.; Grünewald, K. Variable Microtubule Architecture in the Malaria Parasite. *Nat Commun* **2023**, *14* (1), 1216. https://doi.org/10.1038/s41467-023-36627-5.

(7) Gittes, F.; Mickey, B.; Nettleton, J.; Howard, J. Flexural Rigidity of Microtubules and Actin Filaments Measured from Thermal Fluctuations in Shape. *J Cell Biol* **1993**, *120* (4), 923–934. https://doi.org/10.1083/jcb.120.4.923.

(8) Warner, F. D.; Satir, P. The Substructure of Ciliary Microtubules. *J Cell Sci* **1973**, *12* (1), 313–326. https://doi.org/10.1242/jcs.12.1.313.

(9) Khalifa, A. A. Z.; Ichikawa, M.; Dai, D.; Kubo, S.; Black, C. S.; Peri, K.; McAlear, T. S.; Veyron, S.; Yang, S. K.; Vargas, J.; Bechstedt, S.; Trempe, J.-F.; Bui, K. H. The Inner Junction Complex of the Cilia Is an Interaction Hub That Involves Tubulin Post-Translational Modifications. *Elife* **2020**, *9*, e52760. https://doi.org/10.7554/eLife.52760.

(10) Orbach, R.; Howard, J. The Dynamic and Structural Properties of Axonemal Tubulins Support the High Length Stability of Cilia. *Nat Commun* **2019**, *10* (1), 1838. https://doi.org/10.1038/s41467-019-09779-6.

(11) Alvarez Viar, G.; Klena, N.; Martino, F.; Nievergelt, A. P.; Bolognini, D.; Capasso, P.; Pigino, G. Protofilament-Specific Nanopatterns of Tubulin Post-Translational Modifications Regulate the Mechanics of Ciliary Beating. *Curr Biol* **2024**, *34* (19), 4464-4475.e9. https://doi.org/10.1016/j.cub.2024.08.021.

(12) Savage, C.; Hamelin, M.; Culotti, J. G.; Coulson, a; Albertson, D. G.; Chalfie, M. Mec-7 Is a Beta-Tubulin Gene Required for the Production of 15-Protofilament Microtubules in Caenorhabditis Elegans. *Genes & Development* **1989**, *3* (6), 870–881. https://doi.org/10.1101/gad.3.6.870.

(13) Cueva, J. G.; Hsin, J.; Huang, K. C.; Goodman, M. B. Posttranslational Acetylation of α-Tubulin Constrains Protofilament Number in Native Microtubules. *Current Biology* **2012**, *22* (12), 1066–1074. https://doi.org/10.1016/j.cub.2012.05.012.

(14) Black, A. M.; Klocke, M. A.; Zhao, L.; Martin, D. S. Simultaneous Measurement of Microtubule Protofilament Number and Bending Stiffness. *Biophysical Journal* **2012**, *102* (3), 699a–700a. https://doi.org/10.1016/j.bpj.2011.11.3798.

(15) Harris, B. J. Is Microtubule Rigidity Proportional to Protofilament Number? *Biophysical Journal* **2016**, *110* (3), 131a. https://doi.org/10.1016/j.bpj.2015.11.753.
(16) Donhauser, Z. J.; Jobs, W. B.; Binka, E. C. Mechanics of Microtubules: Effects of Protofilament Orientation. *Biophysical Journal* **2010**, *99* (5), 1668. https://doi.org/10.1016/j.bpj.2010.06.065.
(17) Athamneh, A. I. M.; Suter, D. M. Quantifying Mechanical Force in Axonal Growth and Guidance. *Front Cell Neurosci* **2015**, *9*, 359. https://doi.org/10.3389/fncel.2015.00359.
(18) Swaim, G. L.; Glomb, O. V.; Xie, Y.; Emerson, C.; Li, Z.; Beaudet, D.; Hendricks, A. G.; Yogev, S. Axonal Mechanotransduction Drives Cytoskeletal Responses to Physiological Mechanical Forces. *bioRxiv* **2025**, 2025.02.11.637689. https://doi.org/10.1101/2025.02.11.637689.
(19) Shah, K.; Lahiri, D. K. A Tale of the Good and Bad: Remodeling of the Microtubule Network in the Brain by Cdk5. *Mol Neurobiol* **2017**, *54* (3), 2255–2268. https://doi.org/10.1007/s12035-016-9792-7.
(20) Mutalik, S. P.; Ghose, A. Axonal Cytomechanics in Neuronal Development. *J Biosci* **2020**, *45* (1), 64. https://doi.org/10.1007/s12038-020-00029-2.
(21) Motz, C. T.; Kabat, V.; Saxena, T.; Bellamkonda, R. V.; Zhu, C. Neuromechanobiology: An Expanding Field Driven by the Force of Greater Focus. *Adv Healthcare Materials* **2021**, *10* (19), 2100102. https://doi.org/10.1002/adhm.202100102.
(22) Tyler, W. J. The Mechanobiology of Brain Function. *Nat Rev Neurosci* **2012**, *13* (12), 867–878. https://doi.org/10.1038/nrn3383.
(23) Wade, R. H.; Chrétien, D.; Job, D. Characterization of Microtubule Protofilament Numbers. How Does the Surface Lattice Accommodate? *J Mol Biol* **1990**, *212* (4), 775–786. https://doi.org/10.1016/0022-2836(90)90236-F.
(24) Sui, H.; Downing, K. H. Structural Basis of Interprotofilament Interaction and Lateral Deformation of Microtubules. *Structure* **2010**, *18* (8), 1022–1031. https://doi.org/10.1016/j.str.2010.05.010.
(25) Cannariato, M.; Zizzi, E. A.; Pallante, L.; Miceli, M.; Deriu, M. A. Mechanical Communication within the Microtubule through Network-Based Analysis of Tubulin Dynamics. *Biomech Model Mechanobiol* **2024**, *23* (2), 569–579. https://doi.org/10.1007/s10237-023-01792-5.
(26) Cannariato, M.; Zizzi, E. A.; Tuszynski, J. A.; Deriu, M. A. Multiscale Computational Analysis of the Effect of Taxol on Microtubule Mechanics. *ACS Biomater. Sci. Eng.* **2024**, *10* (9), 5666–5674. https://doi.org/10.1021/acsbiomaterials.4c00847.
(27) Deriu, M. A.; Soncini, M.; Orsi, M.; Patel, M.; Essex, J. W.; Montevecchi, F. M.; Redaelli, A. Anisotropic Elastic Network Modeling of Entire Microtubules. *Biophysical Journal* **2010**, *99* (7), 2190–2199. https://doi.org/10.1016/j.bpj.2010.06.070.
(28) Havelka, D.; Deriu, M. A.; Cifra, M.; Kučera, O. Deformation Pattern in Vibrating Microtubule: Structural Mechanics Study Based on an Atomistic Approach. *Sci Rep* **2017**, *7* (1), 4227. https://doi.org/10.1038/s41598-017-04272-w.
(29) Deriu, M. A.; Bidone, T. C.; Mastrangelo, F.; Di Benedetto, G.; Soncini, M.; Montevecchi, F. M.; Morbiducci, U. Biomechanics of Actin Filaments: A Computational Multi-Level Study. *Journal of Biomechanics* **2011**, *44* (4), 630–636. https://doi.org/10.1016/j.jbiomech.2010.11.014.
(30) Memet, E.; Hilitski, F.; Morris, M. A.; Schwenger, W. J.; Dogic, Z.; Mahadevan, L. Microtubules Soften Due to Cross-Sectional Flattening. *eLife* **2018**, *7*, e34695. https://doi.org/10.7554/eLife.34695.
(31) Alushin, G. M.; Lander, G. C.; Kellogg, E. H.; Zhang, R.; Baker, D.; Nogales, E. High-Resolution Microtubule Structures Reveal the Structural Transitions in Aβ-Tubulin upon GTP Hydrolysis. *Cell* **2014**, *157* (5), 1117–1129. https://doi.org/10.1016/j.cell.2014.03.053.
(32) Pettersen, E. F.; Goddard, T. D.; Huang, C. C.; Meng, E. C.; Couch, G. S.; Croll, T. I.; Morris, J. H.; Ferrin, T. E. UCSF ChimeraX : Structure Visualization for Researchers, Educators, and Developers. *Protein Science* **2021**, *30* (1), 70–82. https://doi.org/10.1002/pro.3943.
(33) Olsson, M. H. M.; Søndergaard, C. R.; Rostkowski, M.; Jensen, J. H. PROPKA3: Consistent Treatment of Internal and Surface Residues in Empirical p K a Predictions. *Journal of Chemical Theory and Computation* **2011**, *7* (2), 525–537. https://doi.org/10.1021/ct100578z.
(34) Lindorff-Larsen, K.; Piana, S.; Palmo, K.; Maragakis, P.; Klepeis, J. L.; Dror, R. O.; Shaw, D. E. Improved Side-Chain Torsion Potentials for the Amber ff99SB Protein Force Field. *Proteins* **2010**, *78* (8), 1950–1958. https://doi.org/10.1002/prot.22711.

(35) Wang, J.; Wolf, R. M.; Caldwell, J. W.; Kollman, P. A.; Case, D. A. Development and Testing of a General Amber Force Field. *Journal of Computational Chemistry* **2004**, *25* (9), 1157–1174. https://doi.org/10.1002/jcc.20035.
(36) Jakalian, A.; Jack, D. B.; Bayly, C. I. Fast, Efficient Generation of High-Quality Atomic Charges. AM1-BCC Model: II. Parameterization and Validation. *Journal of Computational Chemistry* **2002**, *23* (16), 1623–1641. https://doi.org/10.1002/jcc.10128.
(37) Berendsen, H. J. C.; Postma, J. P. M.; van Gunsteren, W. F.; DiNola, A.; Haak, J. R. Molecular Dynamics with Coupling to an External Bath. *The Journal of Chemical Physics* **1984**, *81* (8), 3684–3690. https://doi.org/10.1063/1.448118.
(38) Nasedkin, A.; Ermilova, I.; Swenson, J. Atomistic Molecular Dynamics Simulations of Tubulin Heterodimers Explain the Motion of a Microtubule. *Eur Biophys J* **2021**, *50* (7), 927–940. https://doi.org/10.1007/s00249-021-01553-1.
(39) Lindahl; Abraham; Hess; Van Der Spoel. GROMACS 2021.4 Source Code, 2021. https://doi.org/10.5281/ZENODO.5636567.
(40) Igaev, M.; Grubmüller, H. Bending-Torsional Elasticity and Energetics of the plus-End Microtubule Tip. *Proc. Natl. Acad. Sci. U.S.A.* **2022**, *119* (12), e2115516119. https://doi.org/10.1073/pnas.2115516119.
(41) Harris, B. J.; Ross, J.; Hawkins, T. L. Microtubule Seams Are Not Mechanically Weak Defects. *Physical review. E* **2018**, *97 6-1*. https://doi.org/10.1103/PhysRevE.97.062408.
(42) Heinig, M.; Frishman, D. STRIDE: A Web Server for Secondary Structure Assignment from Known Atomic Coordinates of Proteins. *Nucleic Acids Research* **2004**, *32* (Web Server), W500–W502. https://doi.org/10.1093/nar/gkh429.
(43) Salentin, S.; Schreiber, S.; Haupt, V. J.; Adasme, M. F.; Schroeder, M. PLIP: Fully Automated Protein–Ligand Interaction Profiler. *Nucleic Acids Res* **2015**, *43* (W1), W443–W447. https://doi.org/10.1093/nar/gkv315.
(44) Jurrus, E.; Engel, D.; Star, K.; Monson, K.; Brandi, J.; Felberg, L. E.; Brookes, D. H.; Wilson, L.; Chen, J.; Liles, K.; Chun, M.; Li, P.; Gohara, D. W.; Dolinsky, T.; Konecny, R.; Koes, D. R.; Nielsen, J. E.; Head-Gordon, T.; Geng, W.; Krasny, R.; Wei, G.; Holst, M. J.; McCammon, J. A.; Baker, N. A. Improvements to the APBS Biomolecular Solvation Software Suite. *Protein Science* **2018**, *27* (1), 112–128. https://doi.org/10.1002/pro.3280.
(45) Melo, M. C. R.; Bernardi, R. C.; De La Fuente-Nunez, C.; Luthey-Schulten, Z. Generalized Correlation-Based Dynamical Network Analysis: A New High-Performance Approach for Identifying Allosteric Communications in Molecular Dynamics Trajectories. *The Journal of Chemical Physics* **2020**, *153* (13), 134104. https://doi.org/10.1063/5.0018980.
(46) Humphrey, W.; Dalke, A.; Schulten, K. VMD: Visual Molecular Dynamics. *J Mol Graph* **1996**, *14* (1), 33–38, 27–28. https://doi.org/10.1016/0263-7855(96)00018-5.
(47) Meirovitch, L. *Analytical Methods in Vibrations*; Macmillan series in applied mechanics; Macmillan [u.a.]: New York, NY, 1967.
(48) Drabik, P.; Gusarov, S.; Kovalenko, A. Microtubule Stability Studied by Three-Dimensional Molecular Theory of Solvation. *Biophysical journal* **2007**, *92* (2), 394–403. https://doi.org/10.1529/biophysj.106.089987.
(49) Matesanz, R.; Rodríguez-Salarichs, J.; Pera, B.; Canales, Á.; Andreu, J. M.; Jiménez-Barbero, J.; Bras, W.; Nogales, A.; Fang, W.-S.; Díaz, J. F. Modulation of Microtubule Interprotofilament Interactions by Modified Taxanes. *Biophys J* **2011**, *101* (12), 2970–2980. https://doi.org/10.1016/j.bpj.2011.11.005.
(50) Kawaguchi, K.; Yamaguchi, A. Temperature Dependence Rigidity of Non-Taxol Stabilized Single Microtubules. *Biochemical and Biophysical Research Communications* **2010**, *402* (1), 66–69. https://doi.org/10.1016/j.bbrc.2010.09.112.
(51) Hawkins, T. L.; Sept, D.; Mogessie, B.; Straube, A.; Ross, J. L. Mechanical Properties of Doubly Stabilized Microtubule Filaments. *Biophysical Journal* **2013**, *104* (7), 1517–1528. https://doi.org/10.1016/j.bpj.2013.02.026.
(52) Lopez, B. J.; Valentine, M. T. Mechanical Effects of EB1 on Microtubules Depend on GTP Hydrolysis State and Presence of Paclitaxel. *Cytoskeleton* **2014**, *71* (9), 530–541. https://doi.org/10.1002/cm.21190.

(53) Tzima, E.; Kiosses, W. B.; del Pozo, M. A.; Schwartz, M. A. Localized Cdc42 Activation, Detected Using a Novel Assay, Mediates Microtubule Organizing Center Positioning in Endothelial Cells in Response to Fluid Shear Stress. *J Biol Chem* **2003**, *278* (33), 31020–31023. https://doi.org/10.1074/jbc.M301179200.
(54) Moise, K.; Arun, K. M.; Pillai, M.; Salvador, J.; Mehta, A. S.; Goyal, Y.; Iruela-Arispe, M. L. Endothelial Cell Elongation and Alignment in Response to Shear Stress Requires Acetylation of Microtubules. *Front. Physiol.* **2024**, *15*. https://doi.org/10.3389/fphys.2024.1425620.
(55) Chien, S. Mechanical and Chemical Regulation of Endothelial Cell Polarity. *Circulation Research* **2006**, *98* (7), 863–865. https://doi.org/10.1161/01.RES.0000219686.29872.e2.
(56) Kubitschke, H.; Schnauss, J.; Nnetu, K. D.; Warmt, E.; Stange, R.; Kaes, J. Actin and Microtubule Networks Contribute Differently to Cell Response for Small and Large Strains. *New J. Phys.* **2017**, *19* (9), 093003. https://doi.org/10.1088/1367-2630/aa7658.
(57) Galie, P. A.; Oosten, A. van; Chen, C. S.; Janmey, P. A. Application of Multiple Levels of Fluid Shear Stress to Endothelial Cells Plated on Polyacrylamide Gels. *Lab Chip* **2015**, *15* (4), 1205–1212. https://doi.org/10.1039/C4LC01236D.
(58) Nishimura, S.; Nagai, S.; Katoh, M.; Yamashita, H.; Saeki, Y.; Okada, J.; Hisada, T.; Nagai, R.; Sugiura, S. Microtubules Modulate the Stiffness of Cardiomyocytes Against Shear Stress. *Circulation Research* **2006**, *98* (1), 81–87. https://doi.org/10.1161/01.RES.0000197785.51819.e8.
(59) Simmers, M. B.; Pryor, A. W.; Blackman, B. R. Arterial Shear Stress Regulates Endothelial Cell-Directed Migration, Polarity, and Morphology in Confluent Monolayers. *American Journal of Physiology-Heart and Circulatory Physiology* **2007**, *293* (3), H1937–H1946. https://doi.org/10.1152/ajpheart.00534.2007.
(60) Weber, A.; Iturri, J.; Benitez, R.; Zemljic-Jokhadar, S.; Toca-Herrera, J. L. Microtubule Disruption Changes Endothelial Cell Mechanics and Adhesion. *Sci Rep* **2019**, *9* (1), 14903. https://doi.org/10.1038/s41598-019-51024-z.
(61) Mozziconacci, J.; Sandblad, L.; Wachsmuth, M.; Brunner, D.; Karsenti, E. Tubulin Dimers Oligomerize before Their Incorporation into Microtubules. *PloS one* **2008**, *3* (11), e3821. https://doi.org/10.1371/journal.pone.0003821.
(62) Wang, H.; Nogales, E. Nucleotide-Dependent Bending Flexibility of Tubulin Regulates Microtubule Assembly. *Nature* **2005**, *435*, 911–915. https://doi.org/10.1038/nature03606.
(63) Díaz, J.; Andreu, J. Assembly of Purified GDP-Tubulin into Microtubules Induced by Taxol and Taxotere: Reversibility, Ligand Stoichiometry, and Competition. *Biochemistry* **1993**, *32 11*, 2747–2755. https://doi.org/10.1021/BI00062A003.
(64) Pantaloni, D.; Carlier, M.; Simon, C.; Batelier, G. Mechanism of Tubulin Assembly: Role of Rings in the Nucleation Process and of Associated Proteins in the Stabilization of Microtubules. *Biochemistry* **1981**, *20 16*, 4709–4716. https://doi.org/10.1021/BI00519A029.
(65) Chaaban, S.; Brouhard, G. J. A Microtubule Bestiary: Structural Diversity in Tubulin Polymers. *Mol Biol Cell* **2017**, *28* (22), 2924–2931. https://doi.org/10.1091/mbc.E16-05-0271.
(66) Zhang, J.; Guan, S. Tensile Properties of Microtubules: A Study by Nonlinear Molecular Structural Mechanics Modelling. *Physics Letters A* **2020**, *384*. https://doi.org/10.1016/j.physleta.2020.126674.
(67) Schaedel, L.; Triclin, S.; Chrétien, D.; Abrieu, A.; Aumeier, C.; Gaillard, J.; Blanchoin, L.; Théry, M.; John, K. Lattice Defects Induce Microtubule Self-Renewal. *Nature physics* **2018**, *15*, 830–838. https://doi.org/10.1038/s41567-019-0542-4.
(68) Rai, A.; Liu, T.; Katrukha, E.; Estévez-Gallego, J.; Manka, S.; Paterson, I.; Díaz, J.; Kapitein, L.; Moores, C.; Akhmanova, A. Lattice Defects Induced by Microtubule-Stabilizing Agents Exert a Long-Range Effect on Microtubule Growth by Promoting Catastrophes. *Proceedings of the National Academy of Sciences of the United States of America* **2021**, *118*. https://doi.org/10.1073/pnas.2112261118.
(69) Schaedel, L.; John, K.; Gaillard, J.; Nachury, M.; Blanchoin, L.; Théry, M. Microtubules Self-Repair in Response to Mechanical Stress. *Nature materials* **2015**, *14*, 1156–1163. https://doi.org/10.1038/nmat4396.
(70) Jiang, N.; Bailey, M. E.; Burke, J.; Ross, J.; Dima, R. Modeling the Effects of Lattice Defects on Microtubule Breaking and Healing. *Cytoskeleton* **2017**, *74*. https://doi.org/10.1002/cm.21346.

(71) Szatkowski, L.; Merz, D. R.; Jiang, N.; Ejikeme, I.; Belonogov, L.; Ross, J. L.; Dima, R. I. Mechanics of the Microtubule Seam Interface Probed by Molecular Simulations and in Vitro Severing Experiments. *J. Phys. Chem. B* **2019**, *123* (23), 4888–4900. https://doi.org/10.1021/acs.jpcb.9b03059.
(72) Karafyllidis, I. G.; Lagoudas, D. C. Microtubules as Mechanical Force Sensors. *Biosystems* **2007**, *88* (1–2), 137–146. https://doi.org/10.1016/j.biosystems.2006.05.003.
(73) Kalra, A. P.; Patel, S. D.; Bhuiyan, A. F.; Preto, J.; Scheuer, K. G.; Mohammed, U.; Lewis, J. D.; Rezania, V.; Shankar, K.; Tuszynski, J. A. Investigation of the Electrical Properties of Microtubule Ensembles under Cell-Like Conditions. *Nanomaterials* **2020**, *10* (2), 265. https://doi.org/10.3390/nano10020265.